

Unlocking Doping Effects on Altermagnetism in MnTe

Nayana Devaraj,^{1,2,3,*} Anumita Bose,^{3,4} Arindom Das,^{1,2} Md Afsar Reja,³ Arijit Mandal,^{1,2} Awadhesh Narayan,^{3,†} and B. R. K. Nanda^{1,2,‡}

¹*Condensed Matter Theory and Computational Lab,
Department of Physics, IIT Madras, Chennai-600036, India.*

²*Center for Atomistic Modelling and Materials Design, IIT Madras, Chennai-600036, India*

³*Solid State and Structural Chemistry Unit, Indian Institute of Science, Bangalore 560012, India.*

⁴*Scuola Internazionale Superiore di Studi Avanzati (SISSA), I-34136 Trieste, Italy*

(Dated: August 28, 2025)

Governed by specific symmetries, altermagnetism is an emerging field in condensed matter physics, characterized by unique spin-splitting of the bands in the momentum space co-existing with the compensated magnetization as in antiferromagnets. As crystals can have tailored and unintended defects, it is important to gain insights on how altermagnets are affected by the defects-driven symmetry-breaking which, in turn, can build promising perspectives on potential applications. In this study, considering the widely investigated MnTe as a prototype altermagnet, defects are introduced through substitutional doping to create a large configuration space of spin space groups. With the aid of density functional theory calculations, symmetry analysis, and model studies in this configuration space, we demonstrate the generic presence of spin-split of the antiferromagnetic bands in the momentum space. This is indicative of a wider class of *quasi-altermagnetic* materials, augmenting the set of ideal altermagnetic systems. Furthermore, we show that while pristine MnTe does not show anomalous Hall conductivity (AHC) with out-of-plane magnetization, suitable doping can be carried out to obtain finite and varied AHC. Our predictions of quasi-altermagnetism and doping-driven tailored AHC have the potential to open up as-yet-unexplored directions in this developing field.

I. INTRODUCTION

Altermagnetism, a discovery of the present decade as an unconventional magnetic phase, is characterized by the coexistence of a time-reversal symmetry (TRS) breaking and a fully compensated magnetic order [1–3]. It exhibits compensated magnetization, typical characteristics of antiferromagnets, alongside spin-splitting, which was traditionally thought to occur only in ferromagnets. However, the spin-splitting in altermagnets is not of the conventional Zeeman type seen in ferromagnets [3]. Instead, it arises from TRS breaking in systems where oppositely oriented magnetic sublattices are related exclusively by rotational or mirror-symmetry operations. This is in contrast to ferromagnets and antiferromagnets. The former usually consists of a single spin lattice coinciding with the geometrical lattice or a set of distinct sublattices, while the latter is defined as a pair of identical sublattices with opposite spin alignment.

The TRS breaking in altermagnets leads to highly anisotropic spin-splitting in the electronic band structure and Fermi surface, even in the absence of spin-orbit coupling (SOC). The spin-splitting of the bands in altermagnets, generally known as altermagnetic spin-splitting (AMSS), can reach magnitudes similar to those found in ferromagnets [1, 2, 4, 5]. These properties make altermagnets particularly promising for envisaging spin-

tronic applications, as they combine robustness to external magnetic fields with spin-dependent transport phenomena. Their potential for enabling low-dissipation spintronic devices has thus generated considerable interest in both theoretical and experimental research [5–8].

Altermagnetism is predicted in a wide range of material families both in three-dimensional and layered two-dimensional systems. From the electronic structure point of view, they can be seen in metals, semiconductors, insulators, and superconductors [1, 2, 6, 9–11]. Beyond theoretical predictions, experimental demonstrations of altermagnetism have been achieved through momentum-space spectroscopic measurements [12–18]. Among the widely experimentally and theoretically investigated class of altermagnetic compounds are the NiAs prototype crystals, for e.g., metallic CrSb ($T_N = 700$ K), insulating MnTe ($T_N = 310$ K) and NiS ($T_N = 265$ K) [12–14, 17–26]. These *g*-wave altermagnets, having a high Néel temperature, can exhibit large AMSS of the order of 1 eV and hence are promising for band engineering via chemical modifications in order to tune the AMSS and to gain fundamental insights in this emerging area of altermagnetism [1, 7]. With the presence of large SOC and being an insulator, MnTe emerges as an ideal case-study material.

Practical synthesis routes often yield defects and impurities [27–30]. While the conventional charge transport phenomena may not be influenced by such impurities significantly, altermagnetism, being a symmetry-driven phenomenon, is expected to be ultra-sensitive to any kind of symmetry breaking arising from such impurities. Furthermore, doping is often treated as a standard tailoring

* nayanadevaraj@gmail.com

† awadhesh@iisc.ac.in

‡ nandab@iitm.ac.in

mechanism to tune properties. Therefore, since altermagnetism itself is an emerging field, it is very much desirable to have an in-depth understanding of its relationship with defects and doping. Only a few attempts have been made in the literature to study the effect of defects through simplified model Hamiltonians on hypothetical systems [31–34]. However, *ab-initio* electronic structure investigations on real systems are yet to be performed to provide an atomistic and complete picture.

In this study, using density functional theory (DFT) calculations, we investigate how substitutional doping at the non-magnetic Te site influences the altermagnetic properties of MnTe. By designing supercells of MnTe, several doping configurations are created and thereby the DFT results are further analyzed in the context of the underlying symmetries of the doped MnTe systems.

Our results reveal that, although single-atom substitution lowers the system’s symmetry, it does not destroy altermagnetism—regardless of dopant type or position—due to the preserved six fold roto-inversion (S_{6z}) and mirror (M_z) symmetry, which maintains the g -wave altermagnetism. Pair doping leads to a plethora of possible configurations. Within the constraint of $2 \times 2 \times 2$ supercell considered here, there exist 120 possible configurations, which can be classified into five symmetry-based families. Among these, three families (46.66%) retain ideal altermagnetism, while the remaining two lack the necessary rotational or roto-inversion mirror symmetries connecting opposite spin sublattices and instead exhibit quasi-altermagnetic behavior. These quasi-altermagnetic states still show momentum-dependent spin splitting and nearly compensated magnetism. We identify the symmetry-breaking perturbations responsible for the transition from ideal to quasi-altermagnetic states using model Hamiltonian studies. Furthermore, pair-doped structures with lower symmetry exhibit anomalous Hall conductivity (AHC) when magnetization is oriented out-of-plane—a feature absent in pristine MnTe—while a quasi-altermagnetic configuration displays AHC along two different magnetization directions.

Overall, our study reveals how doping influences altermagnetism in MnTe, identifies the conditions and configurations required to preserve it or to break it, and highlights new opportunities for tuning AHC and altermagnetic properties through controlled chemical doping.

II. STRUCTURAL AND COMPUTATIONAL DETAILS

Electronic structure calculations were performed using the Quantum ESPRESSO package [35], which is based on DFT, plane wave basis set, and pseudopotentials. We employed projector augmented wave (PAW) [36] pseudopotentials and the Perdew–Burke–Ernzerhof (PBE) exchange-correlation functional within the generalized gradient approximation (GGA) [37]. A kinetic energy cut-off of 60 Ry was used for the plane-wave basis set.

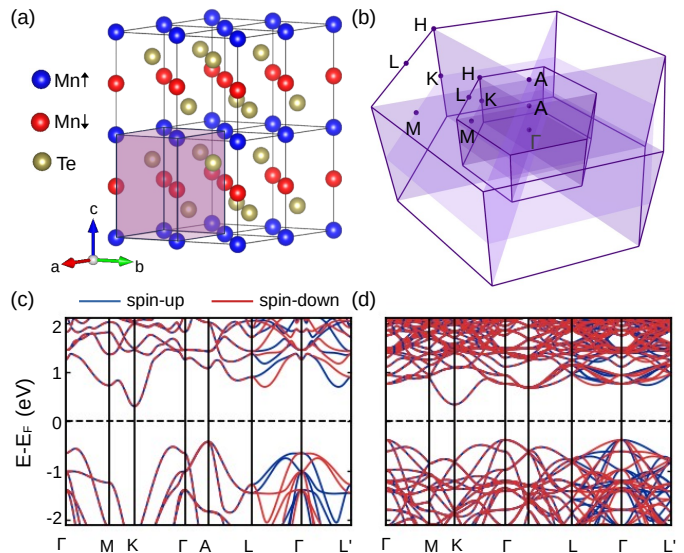


FIG. 1. **Geometric structure and band structure of unit cell and supercell of pristine MnTe.** The $2 \times 2 \times 2$ supercell of MnTe is shown in panel (a), with the unit cell highlighted in purple. The corresponding Brillouin zone for the unit cell and the supercell are shown in panel (b), where the outer and inner zones correspond to unit cell and supercell of MnTe, respectively. As expected, enlarging the real-space crystal reduces the size of the Brillouin zone in reciprocal space. However, since the supercell is formed by doubling the unit cell along all three crystallographic directions, the Brillouin zone retains the same shape, and the high-symmetry k -points of the unit cell can be mapped onto those of the supercell. Panels (c) and (d) show the band structures for the unit cell and the supercell, respectively. These two band structures can be connected by mapping the k -points of their respective Brillouin zones. In both cases, spin-split bands – characteristic of the altermagnetic behavior – are clearly visible along the L – Γ – L' path.

The calculations were performed on various doping configurations Mn(Te,Se/I/Sb) designed out of a $2 \times 2 \times 2$ supercell of MnTe. Structural optimization was conducted using a $5 \times 5 \times 3$ Monkhorst–Pack k -point mesh, while a denser $16 \times 16 \times 10$ k -grid was used to calculate electronic properties. The self-consistent field convergence threshold was set to 10^{-9} Ry. To account for the strong on-site Coulomb interaction of Mn d -electrons, we applied the DFT+ U method [38], with a Hubbard U parameter of 3 eV for the Mn d orbitals, consistent with previous theoretical and experimental studies [19, 39, 40].

AHC was calculated by incorporating SOC within the GGA+ U scheme. Maximally localized Wannier functions, obtained using the Wannier90 code [41], were used to construct a tight-binding Hamiltonian. AHC is then computed using the WannierBerri code [42].

MnTe crystallizes in a hexagonal structure with alternating Mn and Te planes. Within each plane, Mn atoms are ferromagnetically coupled, while adjacent Mn planes are antiferromagnetically aligned along the c -axis, as il-

illustrated in Fig. 1(a). The optimized lattice parameters for MnTe are $a = b = 4.21$ Å and $c = 6.70$ Å, which closely match the experimentally reported values [43]. The $2 \times 2 \times 2$ supercell of MnTe was used to study effect of non-magnetic substitutional doping and is also shown in Fig. 1(a).

III. RESULTS AND ANALYSIS

A. Altermagnetic band structure of pristine MnTe

Hexagonal MnTe is a well-known g -wave altermagnet, characterized by four nodal planes, three parallel to the z -axis and one perpendicular to it, as shown in Fig. 1(b). The electronic bands are degenerate along k -paths that lie within these nodal planes and become non-degenerate along k -paths that lie outside the nodal planes. These non-degenerate bands exhibit AMSS, which varies with momentum and changes sign at opposite momentum directions. This behavior is illustrated in Fig. 1(c), where the band structure along the k -path Γ - M - K - Γ - L (within the nodal plane) is spin-degenerate, while AMSS is observed along L - Γ - L' (outside the nodal planes). Notably, MnTe exhibits a large spin splitting, reaching nearly 1 eV near the valence band maximum. As far as the magnetization is concerned, the Mn atoms of the up (down) sublattice has local spin moments (LSM) of $4.42 \mu_B$ ($-4.42 \mu_B$) resulting in zero net magnetization.

For the substitutional doping discussed later, we have generated a supercell by doubling the unit cell along all three crystallographic directions. Therefore, the corresponding Brillouin zone is shrunk by half in all directions while retaining the shape and the nodal plane of the primitive unit cell [see Fig. 1 (b)]. To obtain a basic understanding of the band structure of the doped system, it is pertinent to view the band structure of the pristine system using the same supercell, which is shown in Fig. 1(d), and equate this with the primitive unit cell band structure shown in Fig. 1(c) through band unfolding. The latter is achieved by mapping the k -point of the supercell Brillouin zone with that of the primitive unit cell and vice versa. Just to cite an example, the high symmetry point A of the unit cell Brillouin zone is folded onto the Γ point of the supercell Brillouin zone. Therefore, the valence band maximum for the case of supercell appears at the point Γ . As expected, since the nodal planes remain unchanged, the AMSS for the supercell are also seen along the path L - Γ - L' .

B. Magnetic structure of MnTe with single non-magnetic atom substitution

To investigate the impact of non-magnetic doping on the altermagnetic properties of hexagonal MnTe, we substituted Te atoms in a $2 \times 2 \times 2$ supercell with Se, I, and Sb. First, we consider the isovalent Se doping with a

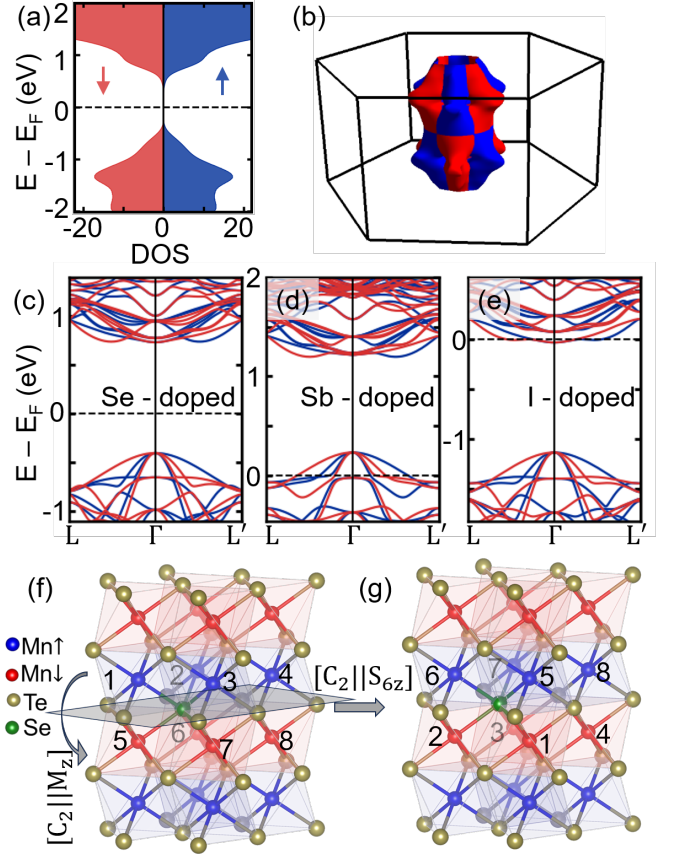


FIG. 2. **Altermagnetism in MnTe supercell with single non-magnetic atom substitution.** The spin-polarized density of states (DOS) of the $2 \times 2 \times 2$ supercell of MnTe with one Te atom substituted by Se is shown in panel (a), where the blue and red colors represent the spin-up and spin-down channels, respectively. The DOS confirms a magnetically compensated state. Panel (b) shows the constant energy surfaces for the spin-up and spin-down channels (blue and red, respectively) at $E = E_F - 0.85$ eV, illustrating the spin-splitting in momentum space. Panels (c)–(e) display the spin-resolved electronic band structures of MnTe supercells with a single Te atom substituted by Se, Sb, and I, respectively. All these structures exhibit momentum-dependent spin-splitting along the L - Γ - L' direction. Panels (f) and (g) illustrate symmetry operations connecting opposite spin sublattices in a single Te-substituted MnTe supercell. The mirror plane perpendicular to the z -axis (M_z), which connects opposite spin sublattices, is present in panel (f). The structures shown in panels (f) and (g) are related by a six-fold rotoinversion symmetry operation (S_{6z}), which consists of a 60° rotation followed by inversion, with the dopant atom serving as the inversion center. Atoms from each sublattice are labeled in planes adjacent to the dopant atom in (f), and their new positions after the S_{6z} operation are shown in panel (g). These features from DFT calculations and symmetry analysis indicate the persistence of g -wave altermagnetism in MnTe upon substitution of a single Te atom.

single substitution corresponding to 6.25% doping concentration. The structurally optimized configuration is shown in Fig. 2(f). The substitution induces notable local structural distortions. In pristine MnTe, the Mn–Mn and Mn–Te bond lengths are 3.35 Å and 2.95 Å, respectively. Upon Se doping, these bonds become non-uniform: Mn–Mn bonds vary between 3.26 Å and 3.38 Å, and Mn–Te bonds range from 2.93 Å to 2.97 Å, while the Mn–Se bond is 2.86 Å.

The local distortions significantly influence the electronic structure and magnetic properties. In pristine MnTe, the Mn atoms of the up (down) sublattice have LSM of 4.42 μ_B (-4.42 μ_B) resulting in a zero net magnetization. In MnTe_{93.75}Se_{6.25}, Mn moments slightly vary from 4.42 to 4.45 μ_B due to the local perturbation induced by doping. However, we find that for a given LSM, there always exists an equal and opposite LSM. Such pairing [as shown in blue and red in Fig. 2(f)] gives rise to zero overall magnetization, as in the pristine case, which is further substantiated from the symmetric spin-resolved density of states (DOS) shown in Fig. 2(a), where the spin-up and spin-down DOS are symmetric at every energy. This naturally raises the point of possible observations of altermagnetism in the doped systems.

In Fig. 2(c), we show the band structure of MnTe_{93.75}Se_{6.25}, along the altermagnetic k -path L - Γ - L' , where we observe spin-dependent splitting of the bands in the momentum space, characteristic of altermagnetism. For the visualization of the altermagnetic behavior in the full Brillouin zone, in Fig. 2(b), we have plotted the constant energy surface for the spin-up (blue) and spin-down (red) bands at $E = E_F - 0.85$ eV. The coexistence of compensated magnetization and momentum-dependent spin-splitting confirms that MnTe retains its altermagnetic character even after substituting one Te atom with Se. To investigate whether the specific site of the Te substitution plays any role in determining this behavior, we performed additional calculations by substituting Se at different Te sites within the supercell. In all cases, the altermagnetic characteristics were preserved, indicating that the observed spin-splitting is intrinsic and independent of the substitution site.

In a recent study, it has been shown that chemical bonding plays a major role in stabilizing and tuning the altermagnetism [25]. Therefore, we further explored the role of dopants by replacing Te with other non-isovalent atoms Sb and I. The respective band structures are shown in Fig. 2(d) and 2(e). Remarkably, in both the cases, we observe characteristic altermagnetic bands. Quantitatively, the substitution induces perturbations that lead to non-uniform magnetic moments among the Mn atoms within the supercell, similar to the Se atom doped case. For the Sb-doped case, Mn magnetic moments range from 4.42 to 4.45 μ_B , and while for I doping, they range from 4.41 to 4.43 μ_B . Despite small local variations, the spin-up and spin-down Mn sublattices remain magnetically compensated in both cases, similar to the case for Se doping, which implies the robustness of the altermag-

netism. This invariance can be explained from a general symmetry perspective, as we illustrate next.

Although magnetic ordering in materials is conventionally studied using magnetic space groups (MSGs), spin space groups (SSGs), where spin and spatial operations are decoupled, have proved to be suitable to characterize altermagnetic materials which exhibit non-relativistic spin-splitting [1, 2, 44]. In the case of MnTe, a collinear altermagnet, spin operations are restricted to either the identity (\mathcal{E}) or time-reversal (C_2), and the symmetry operations connecting opposite spin sublattices are the same in both the SSG and MSG descriptions. Furthermore, since AHC can be explained exclusively within the MSG framework, we employ MSGs for the symmetry analysis in this work.

The space group corresponding to the pristine MnTe is $P6_3/mmc$ (No.194), and corresponding MSG is $P6'_3/m'm'c$ (No.194.268). Maintaining the same supercell geometry, the substitution of one Te atom in MnTe by another element reduces its symmetry, lowering the space group to $P6m2$ (No.187). The corresponding MSG is $P\bar{6}'m'2$ (No.187.211). As a result of doping, the lowering of symmetry generates a larger number of symmetry-inequivalent Mn atoms. Since the Mn atoms exhibit varying LSM, the spin sublattice structure in the doped system is more complex, as shown in Fig. 2(f). Unlike the pristine case, where the up and down spin sublattices consist of only one Mn atom each, the doped system exhibits two spin sublattices, denoted spin-up in blue and spin-down in red, each containing 8 Mn atoms. These atoms are distributed across two different c -planes, with four atoms per plane. The spin-up and spin-down sublattices are related by a mirror symmetry operation (M_z) passing through the central plane, as illustrated in Fig. 2(f). The mirrored sites have equal and opposite LSM. Furthermore, the elements of spin-up and spin-down sublattices are connected through six-fold rotoinversion: a six-fold rotation about the z -axis followed by inversion through the dopant site. To give an example, in Fig. 2(f) and 2(g), we have illustrated how the rotoinversion takes Mn1 to Mn7, Mn2 to Mn5, Mn3 to Mn6, Mn4 to Mn8, and so on. We have further validated that the connecting sites have equal and opposite LSM, leading to a net zero magnetization. Therefore, from the symmetry perspective, this doped system is bound to exhibit altermagnetism. The formation of four nodal planes, three diagonals by rotoinversion (S_{6z}) and one basal (M_{001}) by mirror symmetry leads to the emergence of g -wave altermagnetism in the doped case.

To utilize altermagnetic materials for promising applications, it is imperative to tune the transport as well as the AMSS. The natural way to achieve this is through chemical doping. As mentioned earlier, we have introduced an isovalent doping in the form of Se, hole doping through Sb, and electron doping through I. The respective band structures are shown in Fig. 2 (d),(e). Mn(Te,Se) is an insulator like the pristine compound. However, when the band structures are compared closely,

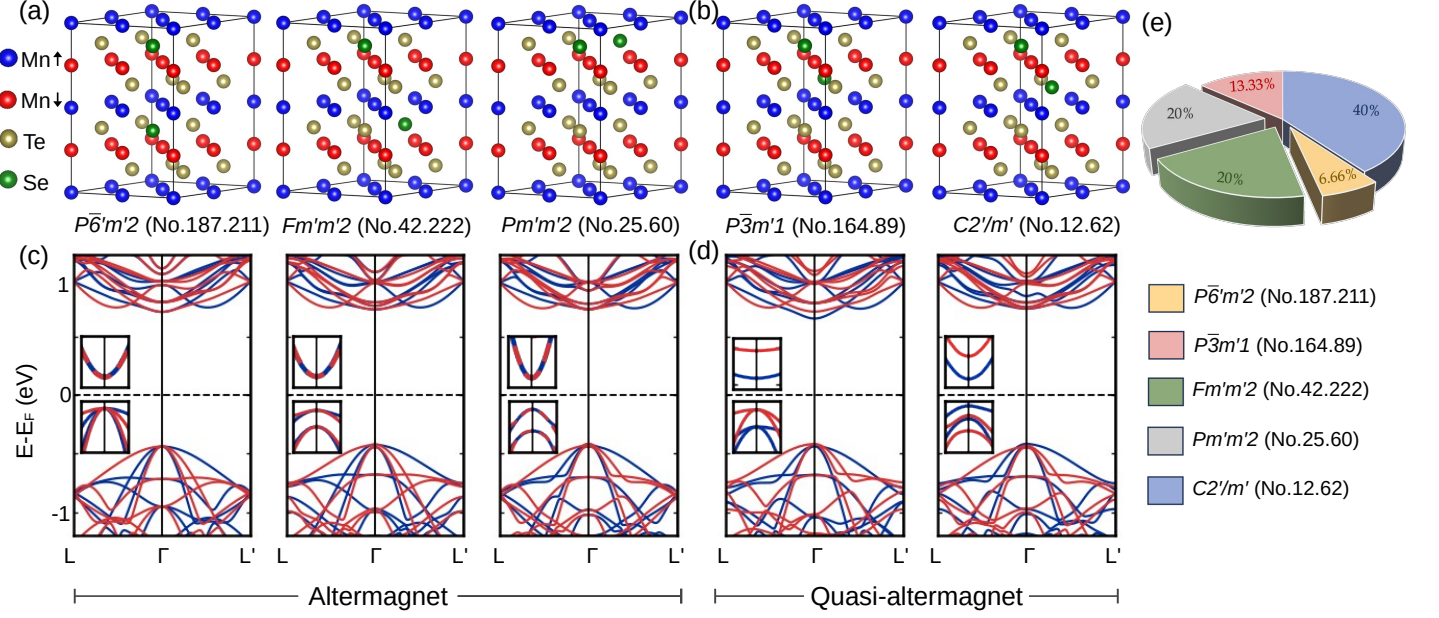


FIG. 3. **Altermagnetic and quasi-altermagnetic states in MnTe for different configurations with a pair of Se substitutions.** Substituting a pair of Te atoms with Se atoms in a $2 \times 2 \times 2$ MnTe supercell yields a system with 12.5% doping. This specific substitution results in 120 unique configurations, distributed among five distinct magnetic space groups (MSGs). The top panel [(a) and (b)] illustrate representative configurations from each MSG, categorized into two classes: (a) those exhibiting ideal altermagnetism, and (b) those displaying quasi-altermagnetic characteristics. The corresponding electronic band structures for these two classes are presented in panels (c) and (d), respectively. The valence and conduction band edges are shown in the insets, where the characteristic features of both altermagnetic and quasi-altermagnetic states are highlighted. Panel (e) provides a pie chart summarizing the distribution of the two-atom-doped configurations across the five MSGs. The gray, green, and yellow segments in the chart represent configurations that exhibit ideal altermagnetism, collectively accounting for approximately 46.66% of the total configurations.

the AMSS is found to be different in the two. We attribute this to different chemical bonding strength [25]. In the case of Mn(Te,Sb) and Mn(Te,I), the hole and electron doping follow the standard semiconductor physics, while retaining the altermagnetism with varying AMSS.

C. Magnetic structure of MnTe for various cases of paired non-magnetic atom substitutions.

Next, we examine the electronic and magnetic structure of the doped system with a pair of dopants to gain further insights. While a single dopant resultant in one configuration irrespective of the position of the dopant in the supercell, a pair of dopants builds a large number of configurations defined by their relative positions. Moreover, a pair of dopants allows us to tailor the symmetry of both geometric and spin space groups, and therefore, we have a wider canvas to further explore the relationship between symmetry and altermagnetism. In the case of MnTe, a pair of dopants at non-magnetic sites gives us 120 possible configurations belonging to five magnetic space group families $C2'/m'$ (No.12.62), $Pm'm'2$ (No.25.60), $Fm'm'2$ (No.42.222), $P3̄m'1$ (No.164.89), and $P6̄m'2$ (No.187.211). In Fig. 3, one representative

configurations from each of these five families and the distributions of the five families are shown. A further detailed symmetry analysis shows that, the configurations belongs to $P6̄m'2$ (No.187.211) has the ideal six-fold roto-inversion making them eligible to be ideal altermagnets, which is also directly validated from our calculated band structures shown in Fig. 3(c). A closer look at the structure reveals that this configuration has the same symmetry as of the single dopant case. However, we find two more families, namely $Pm'm'2$ (No.25.60), $Fm'm'2$ (No.42.222), where the band structures reflect all the characteristic of altermagnetism [see Fig. 3(a)]. Examining these structures further, we find that each of them can be represented through a smaller orthorhombic primitive unit cell with a single dopant in it. These unit cells exhibit two mirror symmetries connecting the opposite spin sublattices, which give rise to d -wave altermagnetism with two nodal planes in the reciprocal space. It is possible to make a transition from d -wave altermagnetism of the primitive unit cell to the g -wave altermagnetism of the supercell, considering that the latter is a hexagonal structure which carries three partially overlapped orthorhombic primitive unit cells (see Appendix- A). The two nodal planes from each of the three orthorhombic substructures lead to four distinct

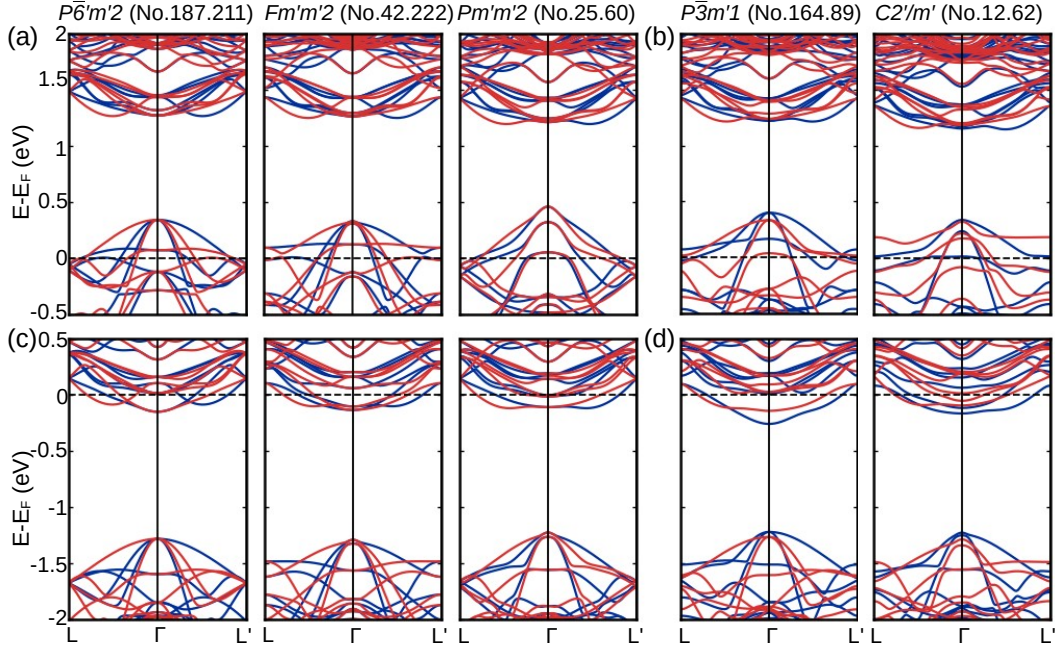


FIG. 4. **Electronic band structures for MnTe supercell with Sb and I pair substitution.** Panels (a) and (b) show the band structures of the MnTe supercell in which a pair of non-magnetic atoms have been substituted with Sb, corresponding to different MSGs. Panels (c) and (d) present the band structures for the MnTe supercell with the same substitution by I. The band structures in (a) and (c) exhibit a perfect altermagnetic character, whereas this feature is absent in (b) and (d). Note the shift of the Fermi level due to non-isovalent doping.

nodal planes, which result in g -wave altermagnetism.

In the remaining two cases, corresponding to $C2'/m'$ (No.12.62) and $P\bar{3}m'1$ (No.164.89), the situation differs from the three cases discussed earlier. Here, the relative positions of the dopants break the symmetry connecting opposite spin sublattices, as they are no longer related by rotation, translation, or inversion. Therefore, in an ideal context, they are no longer altermagnets. However, band structure analysis for the Se-doped case reveals an interesting observation [Fig. 3(d)]: the band structures exhibit a close resemblance to those of altermagnets, including spin-dependent splitting along the altermagnetic k -path, and even though the spin-splitting changes sign, it is not equal on either side of the nodal plane corresponding to the pristine system. We term these *quasi-altermagnetic* materials, augmenting the set of ideal altermagnets. These deviations are evident in these quasi-altermagnetic systems when comparing zoomed views of the valence band maximum and conduction band minimum near Γ across all cases.

Similar to the single-dopant case, we investigate the effects of hole and electron doping for the pair dopant cases. The band structures for the five MSGs doped with Sb (hole-doping) and I (electron-doping) are shown in Fig. 4. For MSGs that display altermagnetism in the isovalent-doping case, Sb and I doping also yield perfect altermagnetism. However, for the other MSGs, deviations from altermagnetic behavior are more pronounced with Sb and I. In the Sb-doped case, the conduction bands, as

expected, show minimal deviation, whereas the valence bands exhibit significant changes. In the I-doped case, deviations occur in both valence band maximum and the conduction band minimum.

Although the ideal altermagnetic condition is broken for MSGs $C2'/m'$ (No.12.62) and $P\bar{3}m'1$ (No.164.89), the net magnetic moment remains nearly zero for isovalent doping and very small for hole and electron doped cases. Band structure analysis along a random path containing both conventional and altermagnetic segments shows that the dominant spin channel alternates between spin-up and spin-down bands in different Brillouin zone regions, resulting in an overall moment close to zero.

D. Anomalous Hall effect in MnTe with paired non-magnetic atom substitutions

The existence of AHC in altermagnets is not inherently guaranteed and depends on the orientation of the Néel vector. In hexagonal MnTe, when the magnetization is aligned along the c -axis, AHC is suppressed due to the presence of symmetry operations such as C_{3z}^{\pm} and in-plane two-fold rotations C_{210} and C_{120} within the MSG $P6_3'/m'm'c$ (No.194.268) [21]. In this section, we investigate the potential for generating a non-zero AHC in MnTe through doping-induced symmetry breaking, based on general symmetry analysis. For a single dopant substitution, or a pair atom substitution with

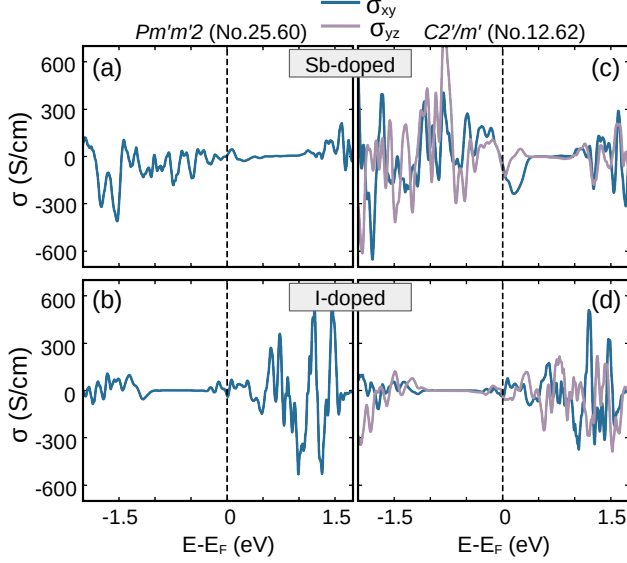


FIG. 5. **Anomalous Hall conductivity of pair doped MnTe with space group $Pm'm'2$ (No.25.60) and $C2'/m'$ (No.12.62).** Panels (a) and (b) show the anomalous Hall conductivity as a function of the Fermi level in pair-doped MnTe with the MSG $Pm'm'2$ (No. 25.60), for Sb and I dopants, respectively. The other two components, σ_{yz} and σ_{xz} , vanish by symmetry. We note that the choice of dopant can effectively tune the magnitude of the anomalous Hall conductivity at the Fermi level. Panel (c) and (d) show the anomalous Hall conductivity for MSG $C2'/m'$ (No.12.62) for Sb and I dopants, respectively. In this case, σ_{yz} and σ_{xz} are non-zero and σ_{xy} vanishes. The change in pair-dopant position alters the active AHC component.

MSG $P\bar{6}'m'2$ (No.187.211), the symmetries that prohibit AHC are retained. However, for other pair doping configurations, with reduced MSG $P\bar{3}m'1$ (No.164.89), a Hall pseudovector along the c -axis becomes symmetry-allowed, as the orthogonal rotation axes combined with time-reversal symmetry (τC_{2x} , τC_{2y}) leave it invariant. In lower-symmetry structures with MSGs $Fm'm'2$ (No.42.222) and $Pm'm'2$ (No.25.60), the presence of the C_{2z} symmetry operation enforces the vanishing of AHC components σ_{yz} and σ_{xz} , while imposing no constraints on σ_{xy} . On the other hand, the lowest-symmetry and the most probable configuration with MSG $C2'/m'2$ (No.12.62) lacks any pure rotational symmetry and retains only the combined symmetry operation τC_{2y} , which permits non-zero components σ_{yz} and σ_{xy} .

While changing the dopant position offers the possibility to tune the direction of the AHC, changing the type of dopant provides a way to tune the magnitude of the AHC near the Fermi level. For instance, Se atoms, which have the same number of valence electrons as Te, preserve the large band gap of MnTe, resulting in a vanishing AHC near the Fermi level. In contrast, doping with Sb or I shifts the Fermi level toward the valence or conduction bands, respectively, leading to finite AHC values at the

Fermi level. In Fig. 5 we show the non-zero components of AHC for candidate materials in two distinct classes of pair non-magnetic atom doped MnTe systems – an altermagnet and a quasi-altermagnet – each incorporating Sb and I atoms as dopants. Top panel illustrates σ_{xy} component in the altermagnetic case with $Pm'm'2$ (No.25.60), where the left (right) one corresponds to Sb (I) doped systems. In the bottom panel, we present two non-zero AHC components – σ_{xy} and σ_{yz} – for quasi-altermagnets with MSG $C2'/m'2$ (No.12.62). Our findings are in agreement with the symmetry considerations discussed previously.

E. Microscopic origin of altermagnetism in doped MnTe: A model Hamiltonian approach

To gain insights into the microscopic origin of formation and dissipation of altermagnetism in doped MnTe, we develop a minimal tight-binding (TB) Hamiltonian based on Slater-Koster (SK) formalism. The SKTB Hamiltonian that exhibits altermagnetism in this class of materials is given by [25],

$$\begin{aligned} \mathcal{H} = & \sum_{i,\mu,\tau,\sigma} \epsilon_{i\mu\tau\sigma} c_{i\mu\tau\sigma}^\dagger c_{i\mu\tau\sigma} \\ & \mp \sum_{i,\mu,\tau,\sigma} (-1)^\tau \Delta_{i,\mu,\tau,\sigma} / 2 c_{i\mu\tau\sigma}^\dagger c_{i\mu\tau\sigma} \\ & + \sum_{i,j,\mu,\nu,\sigma} (t_{i\mu j\nu\sigma} c_{i\mu\sigma}^\dagger c_{j\nu\sigma} + \text{H.c.}), \end{aligned} \quad (1)$$

where, i, j are site indices, μ, ν depict orbital indices, and σ describes the spin indices. $\tau = 1$ represents the sublattice where spin-up states form the majority spin channel, and $\tau = 2$ represents the sublattice where spin-down states form the majority spin channel. The detailed analysis for the chemical bonding origin of altermagnetism in NiAs prototype compounds can be found in Ref. [25]. We primarily focus on the pair doping cases, as single doping is a subset of this. Here, we intend to see the effect of doping in MnTe, which will affect only a part of the existing chemical bonding of the pristine crystal. Since the objective here is to get the underlying mechanism responsible for the presence or absence of altermagnetism and not the full band structure, we created a few quasi-1D crystals as models to study the role of doped atom driven chemical bonding. For further simplicity, we adapted a single orbital model (i.e., one d -orbital from the magnetic atom and one p -orbital from the non-magnetic atom), as the intra-orbital interactions do not have a significant role in the formation of altermagnetism. Here, individual magnetic atoms form the basis for the magnetic sites, while a linear combination of three nearest-neighbor non-magnetic atoms of a given magnetic atom in the same xy -plane form the basis for the non-magnetic sites. We take d_{xy} orbital of the magnetic atom and p_x orbital for the non-magnetic atom as an example. A similar analysis can be carried

out for all other combinations of the orbitals in an analogous manner. Let us next consider the two cases with altermagnetism and quasi-altermagnetism.

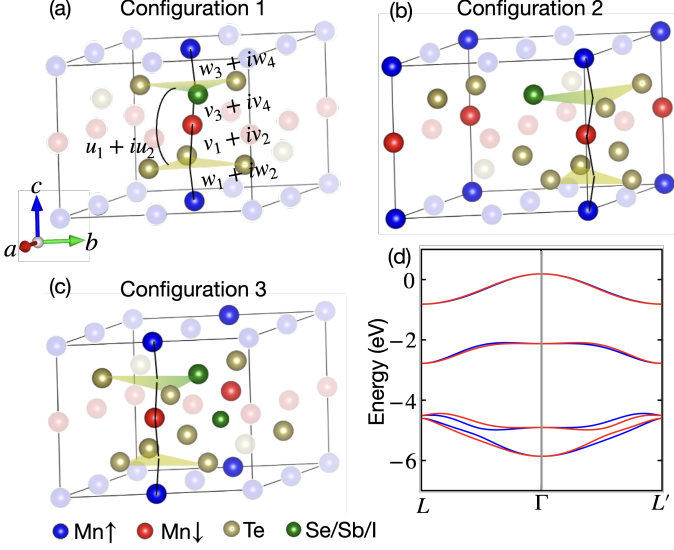


FIG. 6. **SKTB analysis of altermagnetism in MnTe with pair doping.** The primitive unit cell of the representative crystal of MSG $P\bar{6}m'2$ (No.187.211) [see Fig. 3(a)] is considered here. Panels (a)-(c) represent the three quasi-1D configurations (opaque color), which include the doped atoms. The nearest-neighbor non-magnetic coordination of a given magnetic atom is shown by the triangular plane. In (b) and (c), some additional nonmagnetic atoms are generated by employing periodic boundary conditions to represent the quasi-1D chains properly. Panel (d) shows the band structure of configuration 1, where the altermagnetism is not affected by doping, with the expected spin-splitting retained.

Case I: Altermagnetism— Out of five different magnetic space group families of pair doped configurations, $P\bar{6}m'2$ (No.187.211), $Fm'm'2$ (No.42.222), and $Pm'm'2$ (No.25.60) come under this category, where a cell exists with half the volume containing only one doped atom. One representative configuration from each of these families is shown in Fig. 3(a). We consider the crystal structure representing the MSG $P\bar{6}m'2$ (No.187.211) [see Fig. 3(a)] as a prototype to study the effects of chemical doping in this category. Here the doped atoms are placed on top of each other along z and in alternate xy -planes. Therefore, it is possible to build a smaller supercell by reducing the size from $2 \times 2 \times 2$ to $2 \times 2 \times 1$ in this case. As discussed earlier, in the new supercell, there exist four opposite spin pairs of magnetic atoms, and each pair creates a quasi-1D configuration. Out of four such configurations, the nearest neighbor coordination of one

configuration is not affected by the doping, and the corresponding chemical bonding nature remains unchanged. The other three configurations are shown in Fig. 6. The Hamiltonian for these three configurations is written as

$$\mathcal{H}_{4 \times 4}^{\uparrow\uparrow(\downarrow\downarrow)} = \begin{pmatrix} -\left(+\right)\frac{\Delta_{\text{Mn}}}{2} + \alpha & 0 & w_1 + iw_2 & w_3 + iw_4 \\ 0 & +\left(-\right)\frac{\Delta_{\text{Mn}}}{2} + \alpha & v_1 + iv_2 & v_3 + iv_4 \\ w_1 - iw_2 & v_1 - iv_2 & \beta_1 & u_1 + iu_2 \\ w_3 - iw_4 & v_3 - iv_4 & u_1 - iu_2 & \beta_2 \end{pmatrix}. \quad (2)$$

The basis order in the above Hamiltonian is $|\text{Mn} - d\rangle$, $|\text{Mn}' - d\rangle$, $|\text{NM}_{\text{eff}} - p\rangle$, $|\text{NM}'_{\text{eff}} - p\rangle$. Here, $|\text{NM}_{\text{eff}} - p\rangle$ is formed out of all Te atoms, while $|\text{NM}'_{\text{eff}} - p\rangle$ includes one doped atom [see Fig. 6(a-c)]. From the figure, we see that the coordination of the up-spin magnetic atoms is exactly the mirror image of that of the down-spin magnetic atoms. Therefore, the interactions among the magnetic and non-magnetic atoms satisfy the following relations: $w_1^2 + w_2^2 = v_1^2 + v_2^2$ and $w_3^2 + w_4^2 = v_3^2 + v_4^2$. As a result, altermagnetism survives in this case even after chemical doping, as clearly seen in Fig. 6(d).

Case II: Quasi-altermagnetism— As we discussed previously, chemical doping at any other site except the above-mentioned cases, resulted in two magnetic space group families, namely $C2'/m'$ (No.12.62) and $P\bar{3}m'1$ (No.164.89). In these cases, the ideal band dispersion defining altermagnetism disappears [see Fig. 3(b) and (d)]. To investigate the deviation from ideal altermagnetic band dispersion, we take the representative crystal structure of MSG $C2'/m'$ (No.12.62) as a prototype. This system can be divided into four quasi-1D configurations. The coordination of one-fourth of the magnetic atoms in the unit cell is free from doped atoms forming one quasi-1D chain, and thereby, the corresponding chemical bonding remains unaffected. The band structure in these cases can be obtained from the single-band model of pristine MnTe [25]. For another one-fourth of magnetic atoms, which form another quasi-1D chain, the coordination of opposite-spin magnetic atoms can be connected pairwise via a mirror, and the corresponding band structure can be obtained from Eq. 2. These two chains interpenetrate each other and occupy half of the magnetic sites, and the bands formed by them are altermagnetic in nature. The remaining magnetic atoms form the other two quasi-1D chains [see Fig. 7(a) and (b)].

The Hamiltonian describing their band structure can be written as

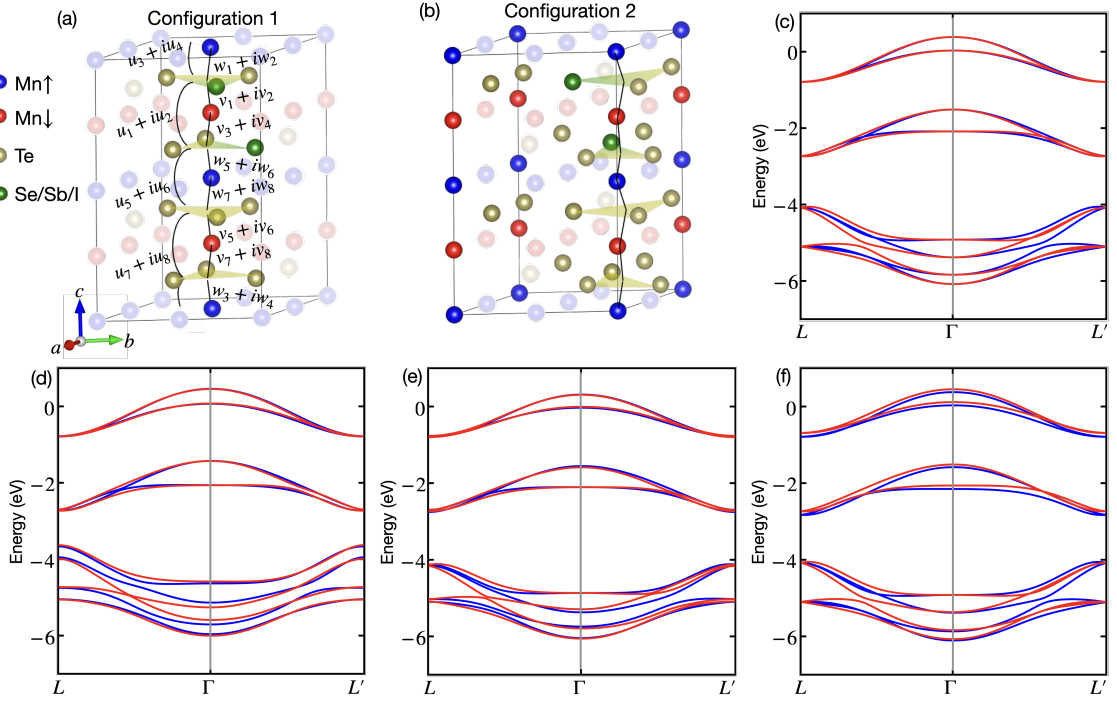


FIG. 7. **SKTB analysis of quasi-altermagnetism in MnTe with pair doping.** The quasi-1D chains are designed out of the representative crystal of MSG $C2'/m'$ (No.12.62) as depicted in Fig. 3(b) to study the effect of doping. Panels (a) and (b) represent the two quasi 1D chains (opaque color) which include the non-magnetic doped atoms. Here also the nearest-neighbor nonmagnetic coordination of a given magnetic atom is shown by the triangular plane, and in (b), a few additional nonmagnetic atoms are generated via the lattice translation vectors to represent the quasi-1D chains properly. Panel (c) showss the altermagnetic band structure for configuration 1 without doping. Panels (d), (e), and (f) represent the quasi-altermagnetic band structure for configuration 1 due to the difference in non-magnetic onsite energies, hopping strengths, and magnetic moments, respectively.

$$\mathcal{H}_{8 \times 8}^{\uparrow\uparrow(\downarrow\downarrow)} = \begin{pmatrix} -(+)\frac{\Delta_{\text{Mn}}}{2} + \alpha & 0 & 0 & 0 & w_1 + iw_2 & 0 & 0 & w_3 + iw_4 \\ 0 & +(-)\frac{\Delta'_{\text{Mn}}}{2} + \alpha & 0 & 0 & v_1 + iv_2 & v_3 + iv_4 & 0 & 0 \\ 0 & 0 & -(+)\frac{\Delta_{\text{Mn}}}{2} + \alpha & 0 & 0 & w_5 + iw_6 & w_7 + iw_8 & 0 \\ 0 & 0 & 0 & +(-)\frac{\Delta'_{\text{Mn}}}{2} + \alpha & 0 & 0 & v_5 + iv_6 & v_7 + iv_8 \\ w_1 - iw_2 & v_1 - iv_2 & 0 & 0 & \beta_1 & u_1 + iu_2 & 0 & u_3 + iu_4 \\ 0 & v_3 - iv_4 & w_5 - iw_6 & 0 & u_1 - iu_2 & \beta_1 & u_5 - iu_6 & 0 \\ 0 & 0 & w_7 - iw_8 & v_5 - iv_6 & 0 & u_5 + iu_6 & \beta_2 & u_7 + iu_8 \\ w_3 - iw_4 & 0 & 0 & v_7 - iv_8 & u_3 - iu_4 & 0 & u_7 - iu_8 & \beta_2 \end{pmatrix}. \quad (3)$$

Here, the basis order is $|\text{Mn}_1 - d\rangle$, $|\text{Mn}_2 - d\rangle$, $|\text{Mn}_3 - d\rangle$, $|\text{Mn}_4 - d\rangle$, $|\text{NM}_{\text{eff1}} - p\rangle$, $|\text{NM}_{\text{eff2}} - p\rangle$, $|\text{NM}_{\text{eff3}} - p\rangle$, $|\text{NM}_{\text{eff4}} - p\rangle$. Each of the non-magnetic effective bases $|\text{NM}_{\text{eff1}} - p\rangle$, $|\text{NM}_{\text{eff2}} - p\rangle$ contains one doped atom, whereas there are no doped atoms in the other two non-magnetic effective bases. The undoped chain exhibits a perfect altermagnetic band structure, as seen in Fig. 7(c). The doped atoms introduce additional perturbations to the non-magnetic onsite energy ($\beta_1 \neq \beta_2$), hopping strengths ($w_1 + iw_2 \neq w_7 + iw_8$, $v_1 + iv_2 \neq v_5 + iv_6$, etc.), and magnetic moments ($\Delta_{\text{Mn}} \neq \Delta'_{\text{Mn}}$). Each perturbation independently lifts the antiferromagnetic sublattice

band degeneracy. In the case of isovalent doping, such as with Se, the difference between β_1 and β_2 is much more prominent than the other two perturbations. In the case of hole-type (Sb) or electron-type (I) doping, each of the perturbations become prominent leading to larger deviation from the ideal altermagnetic band structure, which is substantiated through Fig. 7(d-f). From Fig. 7(d), we see that the difference in the onsite energy of non-magnetic atoms primarily lifts the spin degeneracy of the bands at the Γ point, which is also observed in our DFT-obtained bands, as shown in Fig. 3(b). For the non-isovalent doping cases (i.e., Sb/I doping), the un-

compensated magnetic moments further strengthen the breaking of the degeneracy with larger splitting at the Γ point [see Fig. 4(b) and (d) and Fig. 7(f)]. In addition to this, the non-isovalent doping substantially changes the strengths of hopping interactions, which introduce additional anisotropy to the spin density. Therefore, the bands deviate significantly from the ideal altermagnetic band structure as shown in Fig. 7(e). This is also reflected in our DFT band structures [see Fig. 4(b) and (d)]. Overall, our SKTB models yield a microscopic understanding of the origin of altermagnetism and quasi-altermagnetism in doped MnTe.

IV. SUMMARY

In this study, we have systematically investigated the impact of substitutional doping on the altermagnetic properties of hexagonal MnTe using density functional theory calculations, symmetry analyses, and model Hamiltonians. We found that a single Te-site substitution preserves the altermagnetic character of MnTe regardless of dopant species or substitution site, while enabling effective tuning of its electronic and magnetic properties.

For paired non-magnetic substitutions, the supercell produces 120 possible configurations, and based on their space group symmetries, they are segregated into five different families. We discovered that perfect altermagnetism persists in three families covering $\approx 46\%$ of all possible configurations, while in the remaining two, the opposite-spin sublattices are not rotational-symmetry related and thus do not qualify as ideal altermagnets. However, their band structures retain the key altermagnetic features, including momentum-dependent spin splitting and nearly compensated net magnetization. For isovalent doping, deviations from perfect altermagnetism are minimal, whereas hole and electron doping produce more pronounced deviations, but still result in near-zero magnetization due to alternating spin dominance across the Brillouin zone. We have termed this behavior as quasi-altermagnetism, characterized by significant momentum-dependent spin splitting with a small residual moment. Moreover, through model Hamiltonians, we investigated the microscopic origin of the quasi-altermagnetism and identify the perturbations that lead to the transition from ideal altermagnetism to quasi-altermagnetism.

Our symmetry analyses revealed the possibility of realizing AHC in doped MnTe systems that exhibit both altermagnetism and quasi-altermagnetism, which were further supported by our DFT calculations. Furthermore, our observation opens up a new avenue to engineer a non-zero AHC even for a constant Néel vector direction by changing the chemical composition. This paves the way for experimental detection of AHC and provides a promising route for identifying altermagnetism in insulating MnTe.

In summary, our results identify the general condi-

tions under which altermagnetism persists or deviates under non-magnetic doping, providing a realistic assessment of robustness altermagnets for spintronic applications. Even when ideal symmetry conditions are broken, MnTe retains essential altermagnetic characteristics, and suitable dopant selection offers a viable pathway for tailoring its properties for device integration. We hope that our predictions could be experimentally tested in the near future.

ACKNOWLEDGMENTS

N.D. would like to acknowledge the IoE-IISc post-doctoral fellowship. A.M. thanks MoE India for the PMRF fellowship. M.A.R. is supported by a graduate fellowship of the Indian Institute of Science. A.D. is thankful for the graduate fellowship of the IIT Madras. A.N. acknowledges support from Anusandhan National Research Foundation (ANRF) through grant number CRG/2023/000114.

Appendix A: Altermagnetism in primitive cell of MnTe with paired non-magnetic atom substitutions

Fig. 8 (a) shows the hexagonal MnTe supercell with a pair of non-magnetic atom substitutions, exhibiting MSG $Pm'm'2$ (No. 25.60). The constant energy surfaces for the spin-up and spin-down channels, computed at $E = E_F - 0.7$ eV, are shown in Fig. 8(c). These surfaces reveal a g -wave altermagnetic character, characterized by distinct yet symmetric features connected through a sixfold roto-inversion symmetry in each spin channel.

The primitive cell corresponding to this hexagonal structure is orthorhombic, as illustrated in Fig. 8(b). This orthorhombic unit cell contains half the number of atoms compared to the supercell. It also displays altermagnetic behavior, specifically d -wave altermagnetism, which is evident from the constant energy surfaces of the spin channels shown Fig. 8(d).

The Brillouin zones of both the hexagonal and orthorhombic structures, along with the associated nodal planes, are presented in Fig. 8(e) and (f). The hexagonal structure can be interpreted as a partially overlapped combination of three orthorhombic units [Fig. 8(g)]. Each orthorhombic structure contributes two nodal planes. In the hexagonal configuration, one nodal plane is common to all, while the remaining planes from the individual orthorhombic structures are oriented at 60° with respect to one another, resulting in a total of four nodal planes in the hexagonal Brillouin zone.

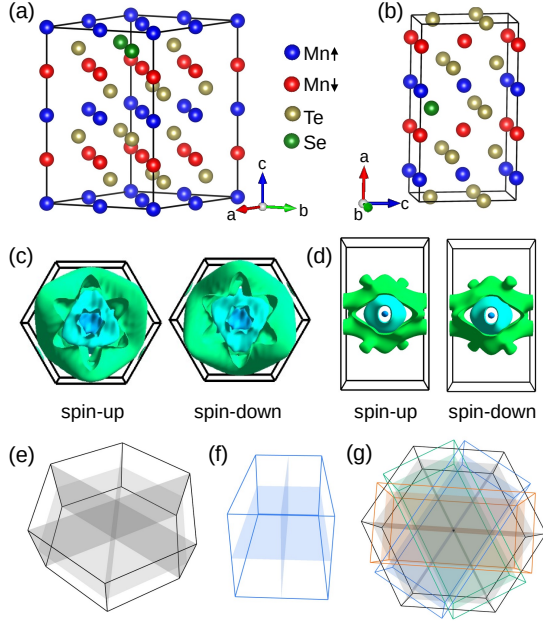


FIG. 8. **Hexagonal supercell and orthorhombic primitive cell of pair non-magnetic atom doped MnTe with MSG: $Pm'm'2$ (No.25.60).** Panel (a) shows the hexagonal MnTe supercell with a pair of non-magnetic atom substitutions, exhibiting MSG $Pm'm'2$ (No.25.60). The corresponding constant energy surfaces for the spin-up and spin-down channels at $E=E_F-0.7$ eV are shown in panel (c), revealing g -wave altermagnetic characteristics. Panel (b) depicts the primitive cell corresponding to the hexagonal structure in (a), and its constant energy surface at $E=E_F-0.7$ eV is presented in panel (d). This structure exhibits d -wave altermagnetism. Panel (e) and (f) correspond to the Brillouin zones of hexagonal and orthorhombic structures and (g) illustrates how three orthorhombic Brillouin zones, colored blue, green, and orange, combine to form a hexagonal Brillouin zone outlined in black. It can be observed that the nodal planes of the three orthorhombic structures collectively give rise to four nodal planes in the hexagonal Brillouin zone, leading to the emergence of g -wave altermagnetism.

Appendix B: Symmetry operations connecting opposite spin sublattices in doped MnTe structures

For the single dopant scenario, the system consistently exhibits altermagnetic ordering. In contrast, the paired dopant scenario leads to several distinct configurations [see Fig. 3(e)], with 46.67% maintaining altermagnetism, while the rest do not. Table I summarizes the symmetry operations connecting the opposite spin sublattices and corresponding magnetic classes for all these doped systems. For MSG $P\bar{6}m'2$ (No.187.211), $Fm'm'2$ (No.42.222), and $Pm'm'2$ (No.25.60) the opposite spin sub-lattices are connected by symmetries other than translation or inversion, therefore being classified as altermagnets. On the other hand, for $P\bar{3}m'1$ (No.164.89) and $C2'/m'2$ (No.12.62), which we refer to as quasi-

TABLE I. **Symmetry operations connecting opposite spin sublattices and AHC components in doped MnTe.** Magnetic space groups (MSGs) obtained from single and pair doping in MnTe, along with the symmetry operations connecting opposite spin sublattices, their corresponding magnetic classes (AM: altermagnet, Q-AM: quasi-altermagnet), and the resulting anomalous Hall conductivity (AHC) components.

MSG	Symmetry between up and down spins	Magnetic class	AHC component
187.211	S_{6z}^{\pm}, M_z	AM	None
164.89	No symmetry	Q-AM	σ_{xy}
42.222	C_{2z}, M_y	AM	σ_{xy}
25.60	C_{2z}, M_x	AM	σ_{xy}
12.62	No symmetry	Q-AM	σ_{xy}, σ_{yz}

altermagnets, there exist no symmetry operations that connect the up and down spin sublattices. This absence results in a lack of compensation between the spin channels, thereby lifting the degeneracy between the up and down spin bands throughout the Brillouin zone.

- [1] L. Šmejkal, J. Sinova, and T. Jungwirth, Beyond conventional ferromagnetism and antiferromagnetism: A phase with nonrelativistic spin and crystal rotation symmetry, *Physical Review X* **12**, 031042 (2022).
- [2] L. Šmejkal, J. Sinova, and T. Jungwirth, Emerging research landscape of altermagnetism, *Physical Review X* **12**, 040501 (2022).
- [3] I. Mazin and P. editors, Altermagnetism—a new punch line of fundamental magnetism (2022).
- [4] L. Šmejkal, R. González-Hernández, T. Jungwirth, and J. Sinova, Crystal time-reversal symmetry breaking and spontaneous hall effect in collinear antiferromagnets, *Science advances* **6**, eaaz8809 (2020).
- [5] C. Song, H. Bai, Z. Zhou, L. Han, H. Reichlova, J. H. Dil, J. Liu, X. Chen, and F. Pan, Altermagnets as a new class of functional materials, *Nature Reviews Materials* , 1 (2025).
- [6] L. Bai, W. Feng, S. Liu, L. Šmejkal, Y. Mokrousov, and Y. Yao, Altermagnetism: Exploring new frontiers in magnetism and spintronics, *Advanced Functional Materials* **34**, 2409327 (2024).
- [7] T. Jungwirth, J. Sinova, P. Wadley, D. Kriegner, H. Reichlova, F. Krizek, H. Ohno, and L. Šmejkal, Altermagnetic spintronics, *arXiv preprint arXiv:2508.09748* (2025).
- [8] R. Tamang, S. Gurung, D. P. Rai, S. Brahimi, and S. Lounis, Altermagnetism and altermagnets: A brief review, *Magnetism* **5**, 17 (2025).
- [9] L. Šmejkal, A. B. Hellenes, R. González-Hernández, J. Sinova, and T. Jungwirth, Giant and tunneling magnetoresistance in unconventional collinear antiferromagnets with nonrelativistic spin-momentum coupling, *Physical*

- Review X **12**, 011028 (2022).
- [10] M. Leiviskä, J. Rial, A. Badura, R. L. Seeger, I. Kounta, S. Beckert, D. Kriegner, I. Joumard, E. Schmoranzarová, J. Sinova, *et al.*, Anisotropy of the anomalous hall effect in the altermagnet candidate $\text{Mn}_{0.5}\text{Si}_{0.3}$ films, arXiv preprint arXiv:2401.02275 (2024).
 - [11] J. González, A. León, C. González-Fuentes, and R. Gallardo, Altermagnetism in two-dimensional Ca_2RuO_4 perovskite, *Nanoscale* (2025).
 - [12] T. Osumi, S. Souma, T. Aoyama, K. Yamauchi, A. Honma, K. Nakayama, T. Takahashi, K. Ohgushi, and T. Sato, Observation of a giant band splitting in altermagnetic MnTe , *Physical Review B* **109**, 115102 (2024).
 - [13] J. Krempaský, L. Šmejkal, S. D'souza, M. Hajlaoui, G. Springholz, K. Uhlířová, F. Alarab, P. Constantinou, V. Strocov, D. Usanov, *et al.*, Altermagnetic lifting of kramers spin degeneracy, *Nature* **626**, 517 (2024).
 - [14] S. Lee, S. Lee, S. Jung, J. Jung, D. Kim, Y. Lee, B. Seok, J. Kim, B. G. Park, L. Šmejkal, *et al.*, Broken kramers degeneracy in altermagnetic MnTe , *Physical review letters* **132**, 036702 (2024).
 - [15] M. Hajlaoui, S. D'Souza, L. Šmejkal, D. Kriegner, G. Krizman, T. Zakusylo, N. Olszowska, O. Caha, J. Michalička, A. Marmodoro, *et al.*, Temperature dependence of relativistic valence band splitting induced by an altermagnetic phase transition, arXiv preprint arXiv:2401.09187 (2024).
 - [16] M. Chilcote, A. R. Mazza, Q. Lu, I. Gray, Q. Tian, Q. Deng, D. Moseley, A.-H. Chen, J. Lapano, J. S. Gardner, *et al.*, Stoichiometry-induced ferromagnetism in altermagnetic candidate MnTe , *Advanced Functional Materials* **34**, 2405829 (2024).
 - [17] S. Reimers, L. Odenbreit, L. Šmejkal, V. N. Strocov, P. Constantinou, A. B. Hellenes, R. Jaeschke Ubierto, W. H. Campos, V. K. Bharadwaj, A. Chakraborty, *et al.*, Direct observation of altermagnetic band splitting in CrSb thin films, *Nature Communications* **15**, 2116 (2024).
 - [18] J. Ding, Z. Jiang, X. Chen, Z. Tao, Z. Liu, T. Li, J. Liu, J. Sun, J. Cheng, J. Liu, *et al.*, Large band splitting in g-wave altermagnet CrSb , *Physical Review Letters* **133**, 206401 (2024).
 - [19] R. D. Gonzalez Betancourt, J. Zubáč, R. Gonzalez-Hernandez, K. Geishendorf, Z. Šobáň, G. Springholz, K. Olejník, L. Šmejkal, J. Sinova, T. Jungwirth, S. T. B. Goennenwein, A. Thomas, H. Reichlová, J. Železný, and D. Kriegner, Spontaneous anomalous hall effect arising from an unconventional compensated magnetic phase in a semiconductor, *Physical Review Letters* **130**, 036702 (2023).
 - [20] O. Amin, A. Dal Din, E. Golias, Y. Niu, A. Zakharov, S. Fromage, C. Fields, S. Heywood, R. Cousins, F. Maccheronzi, *et al.*, Nanoscale imaging and control of altermagnetism in MnTe , *Nature* **636**, 348 (2024).
 - [21] N. Devaraj, A. Bose, and A. Narayan, Interplay of altermagnetism and pressure in hexagonal and orthorhombic MnTe , *Physical Review Materials* **8**, 104407 (2024).
 - [22] G. Yang, Z. Li, S. Yang, J. Li, H. Zheng, W. Zhu, Z. Pan, Y. Xu, S. Cao, W. Zhao, *et al.*, Three-dimensional mapping of the altermagnetic spin splitting in CrSb , *Nature Communications* **16**, 1442 (2025).
 - [23] Y. Bai, X. Xiang, S. Pan, S. Zhang, H. Chen, X. Chen, Z. Han, G. Xu, and F. Xu, Nonlinear field dependence of hall effect and high-mobility multi-carrier transport in an altermagnet CrSb , *Applied Physics Letters* **126** (2025).
 - [24] T. Yu, I. Shahid, P. Liu, D.-F. Shao, X.-Q. Chen, and Y. Sun, Néel vector-dependent anomalous transport in altermagnetic metal CrSb , *npj Quantum Materials* **10**, 47 (2025).
 - [25] A. Mandal, A. Das, and B. Nanda, Deterministic role of chemical bonding in the formation of altermagnetism: Reflection from the correlated electron system NiS , *Physical Review B* **112**, 014420 (2025).
 - [26] A. Hariki, A. Dal Din, O. Amin, T. Yamaguchi, A. Badura, D. Kriegner, K. Edmonds, R. Campion, P. Wadley, D. Backes, *et al.*, X-ray magnetic circular dichroism in altermagnetic $\alpha\text{-MnTe}$, *Physical Review Letters* **132**, 176701 (2024).
 - [27] J. Sambur and J. Brgoch, Unveiling the hidden influence of defects via experiment and data science (2023).
 - [28] J. Pelleg, Defects in materials, in *Diffusion in Ceramics* (Springer, 2015) pp. 21–30.
 - [29] C. G. Van de Walle and A. Janotti, Advances in electronic structure methods for defects and impurities in solids, *physica status solidi (b)* **248**, 19 (2011).
 - [30] P. Muhammad, A. Zada, J. Rashid, S. Hanif, Y. Gao, C. Li, Y. Li, K. Fan, and Y. Wang, Defect engineering in nanocatalysts: from design and synthesis to applications, *Advanced Functional Materials* **34**, 2314686 (2024).
 - [31] J. Gondolf, A. Kreisel, M. Roig, Y. Yu, D. F. Agterberg, and B. M. Andersen, Local signatures of altermagnetism, *Physical Review B* **111**, 174436 (2025).
 - [32] W. Chen, X. Zhou, D. Zhang, Y.-Q. Xu, and W.-K. Lou, Impurity scattering and friedel oscillations in altermagnets, *Physical Review B* **110**, 165413 (2024).
 - [33] A. Maiani and R. S. Souto, Impurity states in altermagnetic superconductors, *Physical Review B* **111**, 224506 (2025).
 - [34] Y.-L. Lee, Magnetic impurities in an altermagnetic metal, *The European Physical Journal B* **98**, 43 (2025).
 - [35] P. Giannozzi, S. Baroni, N. Bonini, M. Calandra, R. Car, C. Cavazzoni, D. Ceresoli, G. L. Chiarotti, M. Cococcioni, I. Dabo, *et al.*, Quantum espresso: a modular and open-source software project for quantum simulations of materials, *Journal of physics: Condensed matter* **21**, 395502 (2009).
 - [36] P. E. Blöchl, Projector augmented-wave method, *Physical review B* **50**, 17953 (1994).
 - [37] J. P. Perdew, K. Burke, and M. Ernzerhof, Generalized gradient approximation made simple, *Physical review letters* **77**, 3865 (1996).
 - [38] M. Cococcioni and S. de Gironcoli, Linear response approach to the calculation of the effective interaction parameters in the $\text{LDA}+u$ method, *Physical Review B* **71**, 035105 (2005).
 - [39] S. Rooj, J. Chakraborty, and N. Ganguli, Hexagonal MnTe with antiferromagnetic spin splitting and hidden rashba–dresselhaus interaction for antiferromagnetic spintronics, *Advanced Physics Research* **3**, 2300050 (2024).
 - [40] W. Szuszkiewicz, E. Dynowska, B. Witkowska, and B. Hennion, Spin-wave measurements on hexagonal MnTe of nias-type structure by inelastic neutron scattering, *Physical Review B* **73**, 104403 (2006).
 - [41] A. A. Mostofi, J. R. Yates, G. Pizzi, Y.-S. Lee, I. Souza, D. Vanderbilt, and N. Marzari, An updated version of wannier90: A tool for obtaining maximally-localised wannier functions, *Computer Physics Communications* **185**, 2309 (2014).

- [42] S. S. Tsirkin, High performance wannier interpolation of berry curvature and related quantities with wannierberri code, npj Computational Materials **7**, 33 (2021).
- [43] J. E. D'Sa, P. Bhoje, K. Priolkar, A. Das, S. Paranjpe, R. Prabhu, and P. Sarode, Low-temperature neutron diffraction study of mnte, Journal of Magnetism and Magnetic Materials **285**, 267 (2005).
- [44] X. Chen, J. Ren, Y. Zhu, Y. Yu, A. Zhang, P. Liu, J. Li, Y. Liu, C. Li, and Q. Liu, Enumeration and representation theory of spin space groups, Physical Review X **14**, 031038 (2024).